

Hierarchically Designed 3D Holey C₂N Aerogels as Bifunctional Oxygen Electrodes for Flexible and Rechargeable Zn-Air Batteries

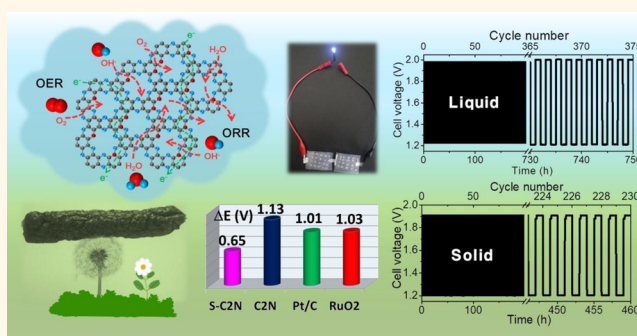
Sambhaji S. Shinde,^{†,||} Chi Ho Lee,^{‡,||} Jin-Young Yu,[†] Dong-Hyung Kim,[†] Sang Uck Lee,^{*,‡,§,||} and Jung-Ho Lee^{*,†,||}

[†]Department of Materials and Chemical Engineering, [‡]Department of Bionano Technology, and [§]Department of Applied Chemistry, Hanyang University, Ansan, Kyungdo 15588, Republic of Korea

S Supporting Information

ABSTRACT: The future of electrochemical energy storage spotlights on the designed formation of highly efficient and robust bifunctional oxygen electrocatalysts that facilitate advanced rechargeable metal-air batteries. We introduce a scalable facile strategy for the construction of a hierarchical three-dimensional sulfur-modulated holey C₂N aerogels (S-C₂NA) as bifunctional catalysts for Zn-air and Li-O₂ batteries. The S-C₂NA exhibited ultrahigh surface area (~1943 m² g⁻¹) and superb electrocatalytic activities with lowest reversible oxygen electrode index ~0.65 V, outperforms the highly active bifunctional and commercial (Pt/C and RuO₂) catalysts. Density functional theory and experimental results reveal that the favorable electronic structure and atomic coordination of holey C–N skeleton enable the reversible oxygen reactions. The resulting Zn-air batteries with liquid electrolytes and the solid-state batteries with S-C₂NA air cathodes exhibit superb energy densities (958 and 862 Wh kg⁻¹), low charge–discharge polarizations, excellent reversibility, and ultralong cycling lives (750 and 460 h) than the commercial Pt/C+RuO₂ catalysts, respectively. Notably, Li-O₂ batteries with S-C₂NA demonstrated an outstanding specific capacity of ~648.7 mA h g⁻¹ and reversible charge–discharge potentials over 200 cycles, illustrating great potential for commercial next-generation rechargeable power sources of flexible electronics.

KEYWORDS: holey C₂N, bifunctional oxygen electrocatalyst, liquid and solid-state Zn-air batteries, Li-O₂ battery, density functional theory



With the ever-increasing demand for flexible and wearable optoelectronic devices and the burgeoning energy and environmental concerns, advanced energy storage systems with high energy densities, superior reliability, and ultralong cycling lives are of great importance.^{1–3} Considerable efforts have been directed to promote flexible lithium-ion batteries and supercapacitors; however, their low energy densities, safety issues, and inadequate cycle lives significantly affect their commercialization.^{4,5} Rechargeable metal (M)-air batteries (M = Zn, Li, Al, Mg, etc.) have become the foci of research because of their high theoretical energy densities (1086–11140 W h kg⁻¹), safety and environmental compatibilities, low costs, and long-term stabilities.^{6–8} Among these, metallic Li and Zn are under intense scrutiny, but resource accessibility and safety illustrate commercialization of Zn-air batteries (ZABs).⁹ Primary alkaline ZABs have already been applied commercially, however, their significant rechargeability is still in the early

stages.^{10,11} The major challenge for air cathodes in aqueous rechargeable ZABs is the large overpotentials and poor oxygen reversibility caused by sluggish oxygen reduction and evolution reactions (ORRs and OERs) during discharging and charging.^{12,13} Precious noble-metal-based (Pt, Ru, Ir, and alloys) electrocatalysts exhibit the best electrocatalytic oxygen performance; however, the scarcity, high prices, and electrochemical instabilities undermine the economic benefits of metal-air batteries.^{14–16} Moreover, dendrite formation, zincate loss at the Zn anode, and carbonate formation at air cathode in liquid electrolytes restrict long-term battery cycling.^{17,18} To address these problems, effective strategies and innovative breakthroughs are critically desirable. Redox mediator is one of the suitable alternatives.¹⁹ On the other hand, solid-state

Received: October 22, 2017

Accepted: December 20, 2017

Published: December 20, 2017

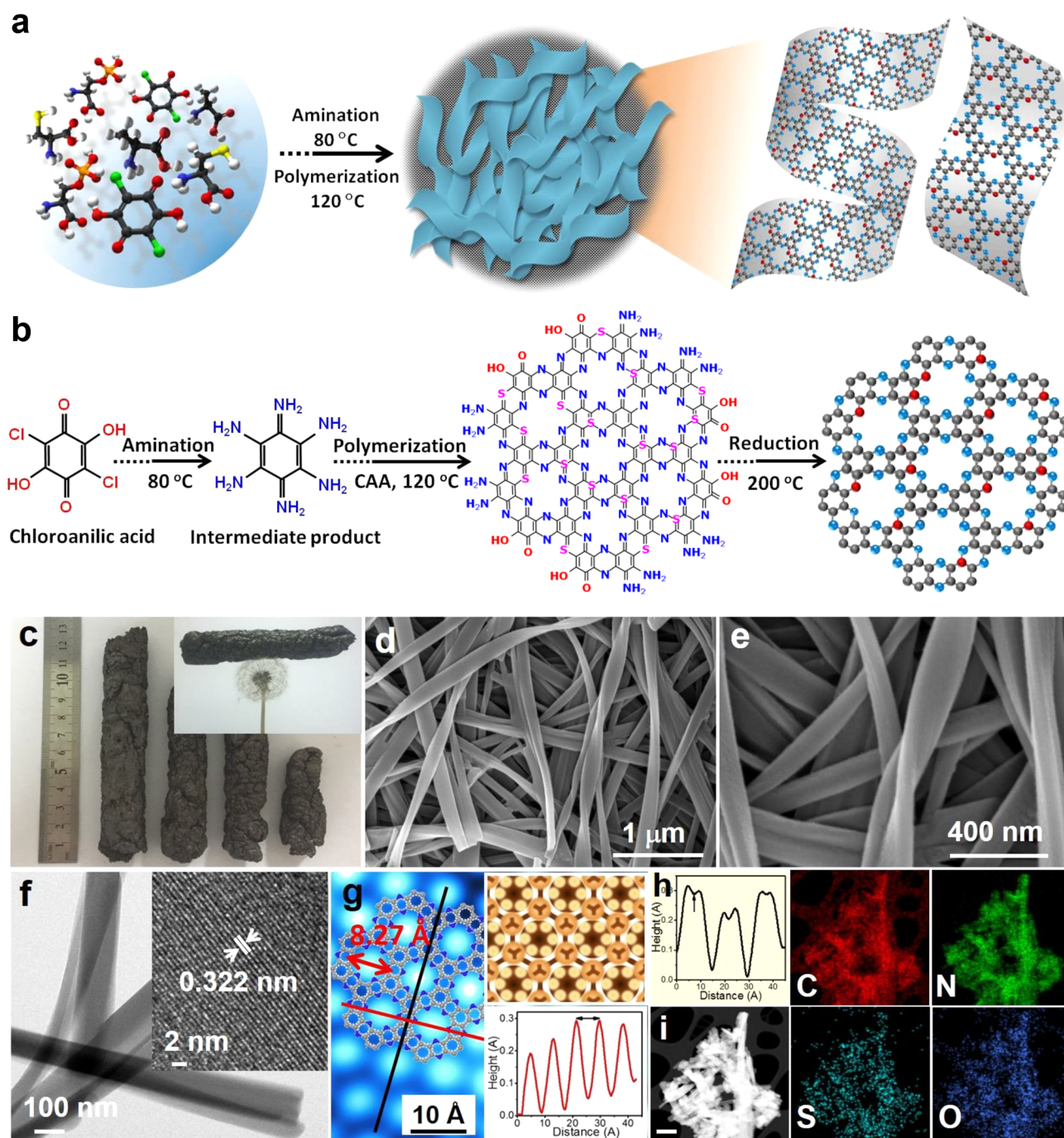


Figure 1. (a) Schematic illustration depicting the development of the 3D holey S-C₂NA bifunctional catalysts through amination and polymerization processes and (b) their reaction mechanism. Chloroanilic acid was aminated to form hierarchical hexaaminobenzene. Each hexaaminobenzene molecule complexed with three chloroanilic acid monomers, L-alanine, and L-cysteine was used as the cross-linker and protic dopant to form the 3D network of the S-C₂N aerogels. (c) Optical image of the fabricated 3D holey S-C₂N aerogel; the inset shows the ultralight aerogel suspended on a dandelion. (d, e) SEM and (f) TEM images of the S-C₂NA catalyst (inset shows the HRTEM image). (g) Atomic-resolution inverted STM image of S-C₂NA on Cu (111). Inset shows the superimposition of S-C₂NA structure (left), atom positions (top-right), and the topographic height profile along the dark red line (down-right). (h) Topographic height profile along the black line, which illustrates the position of the C–N bridged region. (i) HAADF-STEM image of S-C₂NA and the resultant C, N, S, and O element maps (scale bar, 500 nm).

batteries using membrane electrolytes and thin-film electrodes enable mechanically flexible rechargeable ZABs, while providing superior power and energy characteristics as well as electrochemical stabilities.^{3,20,21} Therefore, the development of highly efficient nanostructured bifunctional catalysts and membrane electrolytes with earth-abundant resources, flexible

properties, and competent electrode assemblies is crucial,⁸ can offer incredible advantages over liquid electrolyte systems, and will facilitate significant progress in modern electronics.

Most attempts have been directed toward the development of nonprecious transition-metal-based oxygen catalysts such as metal oxides/sulfides,^{15,22} nitrides,²³ perovskites,^{24,25} spinel/

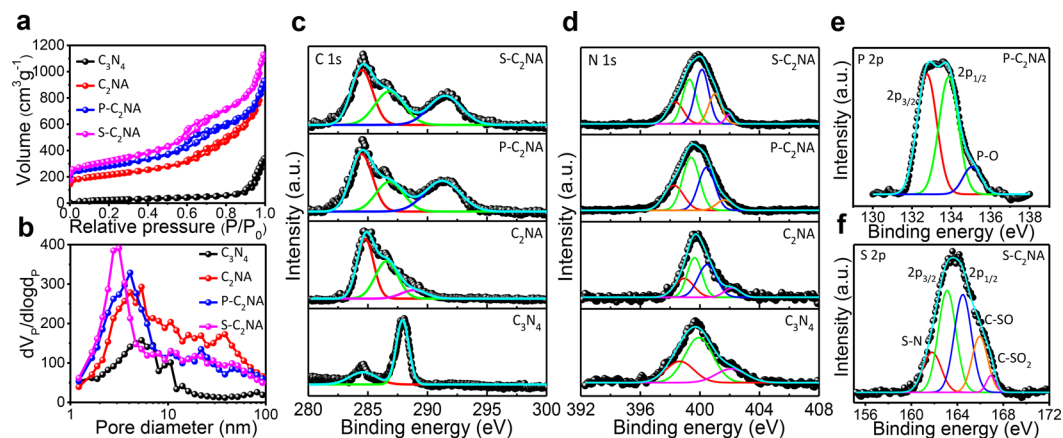


Figure 2. (a) N_2 desorption–adsorption isotherms and (b) the analogous distribution of pores for the pristine C_3N_4 , C_2NA , $P-C_2NA$, and $S-C_2NA$ aerogel catalysts. (c, d) High-resolution C 1s and N 1s XPS spectra of pristine C_3N_4 , C_2NA , $P-C_2NA$, and $S-C_2NA$ catalysts. (e, f) High-resolution P 2p and S 2p XPS spectra of $P-C_2NA$ and $S-C_2NA$ catalyst, respectively.

mixed oxides,²⁶ and carbons^{11,12} to replace noble metals. Among these, porous carbon materials doped with heteroatoms have demonstrated significant interest because of their tunable surface chemistry and fast electron-transfer capacity.^{27–30} However, their disordered and noncoordination pore characteristic limits the electrochemical performance. None of these catalysts are far advanced enough to meet the requirements of practical ZABs (long-term cycling) because of poor conductivity and structural instability at high potentials. The effective strategy to pursue this advancement is to theoretically and experimentally determine the comprehensible interplay among the component structures-properties feature. In this context, relatively ordered porous covalent organic frameworks (COFs, π -conjugated structures), constructed through molecular building blocks with light elements (C, N, O, H, P, B, and S), have attracted enormous attention as metal-free catalysts.^{31,32} Particularly, carbon- and nitrogen-based COFs (holey C_2N) have received significant attention because of their versatile and tunable electronic/chemical functionalities, persistent pore structures with ultrahigh surface areas, strong covalent linkages derived from their building blocks, and high cross-linking densities, that greatly improve structural stability and flexibility.^{33,34} The associated active sites, surface areas, and homogeneous distributions of heteroatoms in COFs strongly promote electron donor–acceptor properties,³⁵ in turn boosting electrocatalytic kinetics. Preservation of mechanical flexibilities and outstanding bifunctional performance of air cathodes for constructing flexible ZABs remains challenging.

A hydrogel is a three-dimensional (3D) hydrophilic cross-linked polymeric network resulting from physical or chemical process, whereas aerogels are 3D porous network replacing liquid hydrogel by air without structural collapse.^{36,37} Aerogels are important in the design of advanced catalysts because of their low densities, large pore volumes, and high surface areas.³⁸ Although carbon nanotubes, cellulose fibers, and graphene have served as hydrogel building blocks, they lack precise control over porosity and building-block dimensions.^{1,39,40} Consequently, the fabrication of aerogels with continual porous structures using COFs building blocks is of significant interest. Herein, we present a template-free scalable fabrication of hierarchical 3D sulfur-modulated holey C_2N aerogels by the simple amination and polymerization of chloroanilic acid (see [Methods](#) and [Supporting Information](#)).

This structure possesses improved oxygen release and mass transport properties, reduced diffusion barriers, and sustained exceptional structural stability upon long-term cycling, while facilitating enhanced penetration of the aqueous electrolyte. The resulting $S-C_2N$ aerogel exhibits outstanding bifunctional performance and improved stability toward the ORR and OER, surpassing those of noble-metal benchmarks, as confirmed by density functional theory (DFT) calculations. The assembled rechargeable ZABs with $S-C_2NA$ air cathodes under liquid and solid-state electrolytes demonstrate excellent electrochemical performance and ultralong cycling lives, outperforming the $Pt/C+RuO_2$ catalyst. Moreover, a Li- O_2 battery with $S-C_2NA$ cathode also showed excellent stability and large specific capacities.

RESULTS AND DISCUSSION

A schematic illustration of the facile two-step template-free strategy for the fabrication of porous 3D sulfur-doped holey C_2N aerogels together with their reaction mechanism is shown in [Figure 1a,b](#). First, chloroanilic acid was aminated with ethylenediamine to produce the intermediate hexaaminobenzene complex (Figures S1 and S2, [Supporting Information](#)). The as-prepared hexaaminobenzene was then polymerized in the presence of chloroanilic acid, L-alanine, and L-cysteine to construct π -conjugated polymeric reinforced C–N structures. After freeze-drying and subsequent pyrolysis, the resultant catalysts forming the array of bifunctional hierarchical holey $S-C_2N$ aerogels (see [Figure S3](#) and experimental methods for details, [Supporting Information](#)). The environmental-friendly sponge-like holey $S-C_2N$ aerogels have the lowest mass density of 64 mg/m^3 and different dimensions ([Figure 1c](#)). Scanning electron microscopy (SEM) images reveal a porous 3D network consisting of hierarchical interweaved twisted nanoribbons ([Figures 1d,e](#)). High-resolution SEM ([Figure 1e](#)) and transmission electron microscopy (TEM, [Figure 1f](#)) reveal nanoribbons with widths in the 150–200 nm range and with lengths of several micrometers. The free internal spaces between neighboring nanoribbons provide abundant electrolyte-accessible interfaces and better diffusion of reactants for fast electrochemical kinetics.⁴¹ High-resolution TEM (inset, [Figure 1f](#)) reveals high crystallinity with a lattice fringe of $\sim 0.322 \text{ nm}$, analogous to the (002) lattice plane of graphitic carbon. Scanning tunneling microscopy (STM) image displays

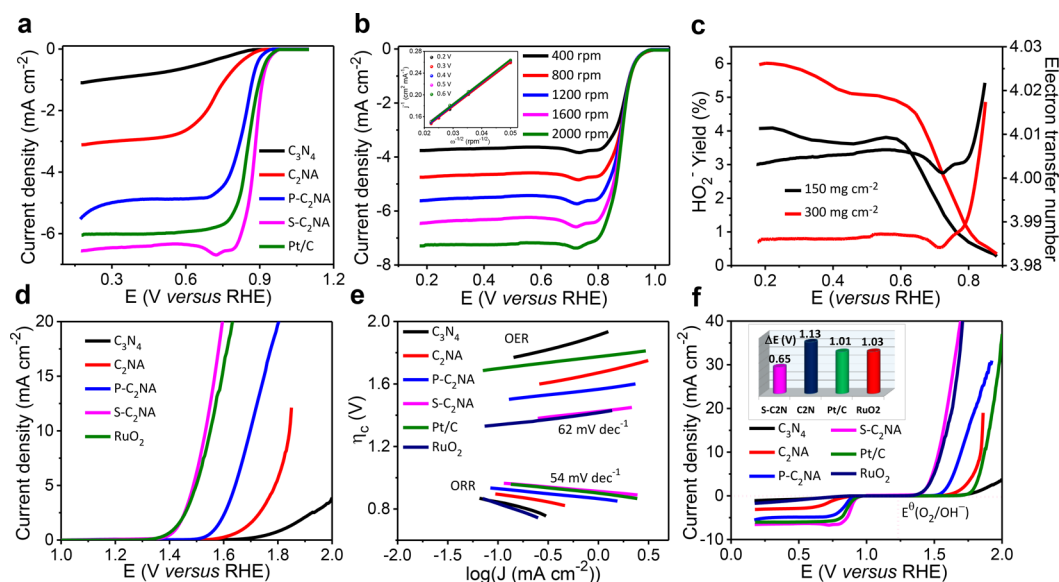


Figure 3. (a) ORR polarization curves (1600 rpm) for the C₂N-based and Pt/C catalysts in O₂-saturated 0.1 M KOH. (b) ORR polarization plots for S-C₂N₄ at various speeds of rotation; the inset shows the resulting K-L plots for different potentials. (c) Peroxide percentage and number of electron transfer for the S-C₂N₄ catalysts as a function of potential in the ORR for different mass loadings. (d) OER polarization plots (1600 rpm, 0.1 M KOH) for different catalysts. (e) Tafel plots determined from (a) and (d). (f) Overall polarization plots (1600 rpm) in the ORR and OER potential windowpane for the C₂N-based, commercial Pt/C, and RuO₂ catalysts (sweep rate: 5 mV s⁻¹); the inset depicts the overall electrocatalytic oxygen performance ($\Delta E = E_{j=10} - E_{1/2}$).

a homogeneously distributed holey structure with hexagonal arrays (left inset, Figure 1g), which is well matched to theoretical holey C₂N system and predicted atom positions (Figures 1b, inset 1g, top-right). The interhole spacing determined from the height profile is $\sim 8.27 \pm 1 \text{ \AA}$ (right inset, Figure 1g). Topographic height discrepancy between hexagonal lattice and holes is $0.29 \pm 0.09 \text{ \AA}$ (Figure 1h), and the observed benzene rings are slightly elevated than C–N bridging regions, confirming smaller interplanar distances than graphite.⁴² Furthermore, the expansion/contraction in height profiles confirms the generation of defect sites because of sulfur doping in the C₂N host lattice. Moreover, STEM and the corresponding elemental maps (Figure 1i) confirm the homogeneous spatial distributions of C, N, O, and S for the S-C₂N aerogels. Inductively coupled plasma (ICP) analysis confirms the 2:1 atomic ratio of C to N in the pristine C₂NA, well consistent with the EDS and XPS results. X-ray diffraction (XRD), thermogravimetric analysis (TGA), and Fourier transform infrared (FTIR) spectroscopy (Figures S4–S6, Supporting Information) indicate the amination and polymerization processes produced thermally stable COFs domains (holey C₂N) doped with P or S from chloroanilic acid, L-phosphoserine, or L-cysteine, respectively. The template-free chemical process employed here generates abundant graphitic edge-sites, facilitating large surface areas for enhanced oxygen reactions, and suggests large-scale manufacturing because of precursor accessibility and process simplicity.

Nitrogen sorption experiments were performed to determine the surface areas and pore structures of the C₂N-based aerogels (Figure 2a,b). The Brunauer–Emmett–Teller (BET) surface areas of pristine C₃N₄, C₂NA, P-C₂NA, and S-C₂NA were 129, 1145, 1468, and 1943 m² g⁻¹, respectively, which is much higher than those of hard-templated porous carbons and other catalysts (~ 400 – $1500 \text{ m}^2 \text{ g}^{-1}$).^{2,3,11,12,43,44} All catalysts resemble type-IV isotherms with characteristic H3 hystereses (Figure 2a), illustrating the presence of micro- and

mesopores.^{2,11} Such micro/mesopores were confirmed from the Barrett–Joyner–Halenda (BJH) pore-distribution profiles (Figure 2b), which exhibit sharp peaks at $< 3 \text{ nm}$. A significantly enhanced pore volume of $1.56 \text{ cm}^3 \text{ g}^{-1}$ was observed for S-C₂N aerogels compared to C₃N₄ ($0.21 \text{ cm}^3 \text{ g}^{-1}$). The ultrahigh surface areas and pore volumes of the 3D aerogels are anticipated to provide highly dense active sites and favorable mass transfer, facilitating enhanced electrocatalytic activity.

The chemical oxidation states and elemental compositions of the catalysts were examined by X-ray photoelectron spectroscopy (XPS). The XPS survey spectra of the C₂N-based aerogels exhibit the presence of peaks corresponding to carbon, nitrogen, oxygen, phosphorus, and sulfur in the desired stoichiometric ratios, confirming the formation of metal-free catalysts (Figure S7, Table S1, Supporting Information). High-resolution C 1s spectra of the C₂N-based aerogels (Figure 2c) reveal three characteristic peaks of sp² graphitic C=C, C–N, and C-heteroatoms bonding at 284.5, 286.6, and 291.4 eV, respectively.⁴² The absence of C–N coordinated peak (288.1 eV) originating from the s-triazine of pristine C₃N₄ confirms that holey C₂N aerogels had successfully been formed. Notably, the electron conductivities of C₂N catalysts were reinforced because of their high sp²-carbon contents that are favorable for enhanced ORR and OER activities.⁴⁵ The N 1s spectra of the C₂N-based aerogels (Figure 2d) exhibit five characteristic nitrogen-moiety peaks at 398.4 (pyridinic, N1), 399.3 (pyrrolic, N2), 400.14 (graphitic, N3), 401.10 (quaternary, N4), and 402.12 eV (oxidized pyridinic, N⁺O⁻, N5), respectively.⁴⁶ The presence of graphitic and quaternary nitrogens in the C₂N-based aerogels compared to C₃N₄ is a result of *in situ* activation through amination, which explains the degree of graphitization.⁹ The pronounced shifts in N species compared to C₂N confirm the existence of S–N–C or P–N–C in the C₂N matrices.²³ Quantified nitrogen normalized percentages are summarized in Figure S8 and

Table S2 (Supporting Information). Note that the nitrogen moieties establish different electronic/chemical environments with neighboring carbon atoms resulting in different electrocatalytic activities.¹¹ Hence, the co-existence of pyridinic and graphitic, as well as pyrrolic/pyridine, quaternary, and oxidized nitrogen moieties in S-C₂NA endows outstanding catalytic performance toward oxygen reactions. The P 2p spectrum (Figure 2e) displays three distinguishable peaks; a doublet corresponding to P bound to conjugated aromatic C (P–C at 132.7 and 133.8 eV) and P–O bonding (135.1 eV), respectively.⁴⁷ The peak centered at 133.8 eV corresponds to P–N coordination, illustrating that P has replaced C in P-C₂NA to produce P–N bonds that can serve as ORR active sites.⁴⁸ Figure 2f displays the S 2p spectrum of the S-C₂N aerogel, which exhibits spin–orbit split peaks at 163.1 and 164.5 eV assigned to S 2p_{3/2} and S 2p_{1/2} that originate from the sulfur in thiol and thiophene, respectively. Another fitted signal at 161.8 eV is consistent with N–S bonding, whereas minor peaks observed at 165.9 and 166.9 eV indicate the presence of benzothiadiazole-sulfur and oxidized-sulfur species (C–SO_x–C).^{27,49} Notably, the existence of thiophene-like structures and S–N bonding to neighboring carbon atoms in S-C₂N aerogels,⁴⁹ implying the formation of C–S–C and C–N–S structures by replacing S heteroatoms to C and/or N atoms that exhibit active centers for considerable catalytic performance as predicted by DFT calculations (*vide infra*). These results confirm the successful dispersion of atomic P or S throughout the C₂N networks resulting from polymerization. The quantitative analysis of sulfur concentrations is shown in Figure S9 and Table S3 (Supporting Information). Overall, the presence of various surface functional groups with P or S doping in the holey C₂N nanostructures can facilitate enhanced electrocatalysis.

The ORR/OER bifunctional electrocatalytic performance of holey C₂N-based aerogels was investigated in alkaline electrolyte (0.1 M KOH) using a three-electrode cell in comparison with noble metal Pt/C and RuO₂ catalysts (Figure S10, Supporting Information). Cyclic voltammograms of all the C₂N-based aerogels demonstrate well-defined cathodic peaks in O₂-saturated KOH electrolyte, whereas no redox peak in the N₂-saturated electrolyte (Figure S11, Supporting Information). The reduction potential observed for S-C₂NA (0.86 V) is more positive than those of Pt/C (0.85 V), P-C₂NA (0.82 V), and C₂NA (0.79 V), illustrating the exceptional catalytic ORR activity of metal-free S-C₂NA. Moreover, a similar trend is observed for the current densities, which indicates that S-C₂NA is more active than either P-C₂NA or C₂NA. Notably, the ultrahigh surface area (Figure 2a), high graphitization, and abundant active sites generated by heteroatoms doping in the C₂N system are favorable for ORR performance. Rotating disc electrode (RDE) polarization curves for C₂N-based aerogels are displayed in Figure 3a. Extraordinarily, the S-C₂N aerogel displays a high onset potential of 0.98 V, a half-wave potential ($E_{1/2}$) of 0.88 V, and a limiting current density (J) of 6.6 mA cm⁻²; the S-C₂N aerogel outperforms Pt/C (onset potential = 0.96 V, $E_{1/2}$ = 0.85 V, and J = 6.03 mA cm⁻²) and recently reported metal-free and metal-based catalysts (Table S4, Supporting Information).^{1,2,11–13,39,47} The anomalous peak observed at ~0.72 V stemmed from the presence of sulfur in thiol groups in S-C₂NA catalysts, shown in XPS spectra (Figure 2f), boosting the ORR activity.^{50,51} The best ORR and OER performances were observed at the 6 at% S-C₂NA in comparison to other sulfur concentrations (Figure S12,

Supporting Information). S-C₂NA exhibited the highest ORR catalytic performance among the aforementioned C₂N-based aerogels in terms of limiting current and onset and half-wave potentials, highlighting the synergistic effect of its hierarchical holey structure, intrinsic N, and S doping, and smaller charge-transfer resistance (Figure S13, Supporting Information). The number of electrons transferred per oxygen (n) in the ORR was determined by linear-sweep voltammetry (LSV) (Figure 3b) rendering to the Koutechy–Levich (K-L) equation. The K-L profiles (inset, Figure 3b) display linear increases in current density with increasing speed of rotation, indicative of first-order reaction kinetics toward dissolved oxygen. The number of electrons transferred for S-C₂NA was calculated to be ~4, analogous to that of Pt/C (Figure S14, Supporting Information), and demonstrates fast kinetics through the desired four-electron-transfer ORR pathway.¹² The peroxide percentage (HO₂⁻) and n were further examined from the disk and ring currents, respectively (Figure S15a, Supporting Information). The HO₂⁻ yield for the S-C₂N aerogel remained below 6% over all potentials, with n ranging from 3.98 to 4.02 (Figure 3c), which is comparable to the Pt/C. The quantified 4e⁻ transfer process and substantially lower HO₂⁻ yield confirm the preferred oxygen reduction kinetics involves from the direct reduction of O₂ into H₂O. Overall, the enhanced ORR activity is attributed to the nitrogen content and preferred coordination along the pore openings (abundant edge sites), playing a significant role in decreasing the overpotentials of the C₂N-based catalysts. The difference in electronegativities of N and C atoms enables for the oxygen adsorption on the surface of carbon. In general, the pyridinic and graphitic N species generate the desired unsaturated coordination sites along the pore sites in C structure, displaying most active sites for the ORR.^{52,53} Mainly, the S-C₂NA possesses 55% of pyridinic plus graphitic N contribution as compared to the overall nitrogen content, larger than other C₂NA-based catalysts (~51%). It induces charge redistribution in the π -conjugated system possessing reduced energy barriers for ORR. Furthermore, the additional major active moiety in S-C₂NA is quaternary N showing contribution of 17%. Quaternary N is able to deliver electrons to π -conjugated coordination facilitating an improved nucleophile strength of the neighboring C rings [C(δ^-)] in order to increase the adsorption of oxygen intermediates (O* and OOH*) {due to a high density of lone pair electrons in oxygen[O(δ^+)]}; therefore, boosting the ORR.^{53–55} Energetically unfavorable pyrrolic N is comparatively higher in the C₂NA and P-C₂NA than in the S-C₂NA generated in the form of amine or cyano groups, suggesting lower ORR activity.⁵⁶ Thus, the co-existence of pyridinic-, graphitic-, and quaternary-types of N in S-C₂NA is matched well with the improvement of observed ORR performances. Desired increments in density and coordination of N sites can be realized from the successful formation of holey structure.

To evaluate the bifunctionality of the C₂N-based aerogels, the OER performance was also analyzed through LSV profiles (Figure 3d). The overpotentials determined at a current density of 10 mA cm⁻² follow the order: S-C₂NA (0.3 V) < RuO₂ (0.32 V) < P-C₂NA (0.47 V) < C₂NA (0.61 V) and are better than those previously reported OER catalysts (Table S4, Supporting Information).^{1,2,11,12} S-C₂NA displayed the highest current density (20.97 mA cm⁻²) compared to those of RuO₂ (15.6 mA cm⁻²), P-C₂NA (2.16 mA cm⁻²), and C₂NA (0.3 mA cm⁻²) at a potential of 1.6 V (*vs* RHE). Additionally, S-

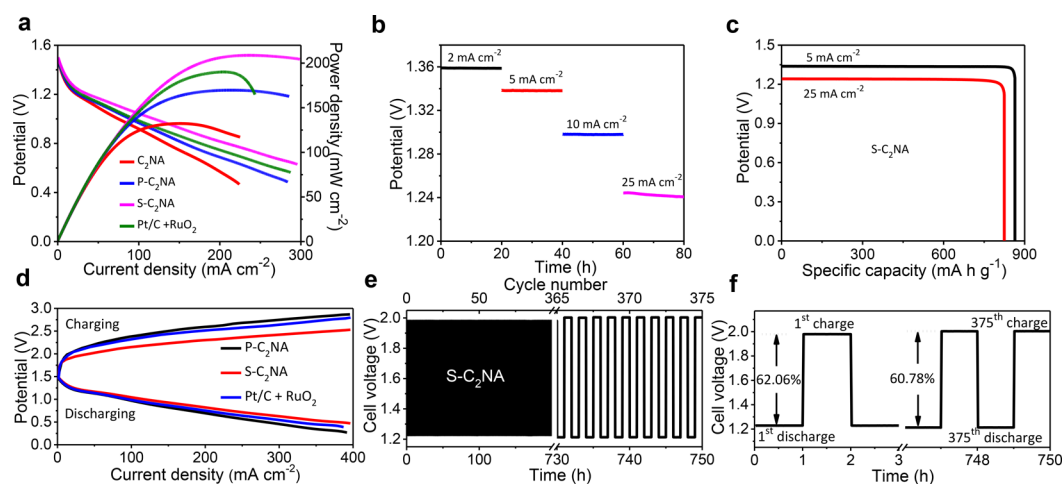


Figure 4. (a) Discharge polarization and power-density plots of ZABs with C₂NA-based and commercial Pt/C cathodes in KOH electrolyte. (b) Discharge curves of the S-C₂NA based ZABs for different current densities. (c) Specific capacities for ZABs with S-C₂NA cathodes normalized to the consumed mass of Zn at current densities of 5 and 25 mA cm⁻². (d) Discharging and charging polarization plots for Pt/C + RuO₂, P-C₂NA and S-C₂NA. (e, f) Galvanostatic discharging and charging voltage profiles of the rechargeable ZAB with a bifunctional S-C₂NA catalyst for 10 mA cm⁻² current density.

C₂NA exhibited the smallest onset potential (1.28 V) compared to RuO₂ (1.32 V) and the remaining C₂NA-based catalysts. Figure 3e reveals that S-C₂NA has the smallest Tafel slope (54 mV dec⁻¹) within the ORR region compared to Pt/C (72 mV dec⁻¹), P-C₂NA (68 mV dec⁻¹), and C₂NA (107 mV dec⁻¹); S-C₂NA also exhibits a lower Tafel value of 62 mV dec⁻¹ in the OER region than RuO₂ (78 mV dec⁻¹) and other reported catalysts, confirming the outstanding bifunctional electrochemical performance with similar ORR and OER rate-determining steps consistent with DFT calculations (*vide infra*). The overall reversibility and oxygen electrode performance index were assessed by the variance of OER and ORR metrics: $\Delta E = E_{j=10} - E_{1/2}$, where $E_{j=10}$ is the OER operating voltage at 10 mA cm⁻², and $E_{1/2}$ is the ORR half-wave potential.^{2,23} The smaller the ΔE value, the greater bifunctional performance the catalyst has.⁵⁷ S-C₂NA demonstrated the smallest ΔE value of 0.65 V (Figure 3f), which notably outperforms the noble-metal benchmarks Pt/C (1.01 V), RuO₂ (1.03 V), and previously reported highly active state-of-the-art metal, as well as metal-free, bifunctional catalysts (Table S4, Supporting Information), highlighting the superior bifunctional performance of the S-C₂N aerogels for ORR and OER.

Apart from excellent bifunctional performance, catalyst stability is another critical parameter that affects the cycle lives of ZABs. The ORR chronoamperometric responses (Figure S15b, Supporting Information) reveal a significant decline in current density for commercial Pt/C (18.45%), whereas the current density of S-C₂NA retains unchanged over 10 h of continuous operation. Moreover, Pt/C displays a distinct methanol oxidation current, however no obvious change is observed for S-C₂NA with a methanol crossover effect, confirming their strong methanol tolerance, corrosion resistance, and selectivity to ORR (Figure S15c, Supporting Information). S-C₂NA also demonstrated excellent resistance against CO poisoning (without any current density change) compared to Pt/C (Figure S15d, Supporting Information). Moreover, the S-C₂NA showed a slight change in half-wave potential (8 mV) and almost no change in active surface area after 5000 cycles; however, Pt/C exhibited loss in half-wave

potential (83 mV) and active surface area (26%) under the same accelerated durability test (Figure S16, Supporting Information). The OER polarization profiles of RuO₂ exhibit a gradual increase in overpotential by 0.13 V, whereas negligible deterioration was recorded for S-C₂NA after 1000 cycles. Moreover, the chronoamperometric plots reveal that S-C₂NA retains 99.65% of its original current density, whereas 23.1% current loss was observed for RuO₂ within 10 h (Figure S17, Supporting Information), illustrating the superior stability over noble metals in alkaline medium. The robustness, flexibility, and easy release of oxygen bubbles generated during the OER from the S-C₂NA electrode is demonstrated in Video S1 (Supporting Information). The outstanding ORR/OER bifunctional activity and stability of S-C₂NA makes it a highly promising catalyst for alkaline and flexible metal-air batteries.

Building on the promising bifunctional performance of S-C₂N aerogels, we constructed a conventional ZAB (Figure S18, Supporting Information) using the S-C₂N aerogels and a Zn plate as the air cathode and anode, respectively, with 6 M KOH in 0.2 M zinc acetate as electrolyte, in comparison with noble-metal catalyst Pt/C+RuO₂. The open-circuit voltage (OCV) observed for S-C₂NA reached 1.49 V and is comparable to that of the Pt/C+RuO₂ (Figure 4a). The polarization profiles (Figure 4a) reveal a discharge voltage for S-C₂NA that surpasses that of Pt/C+RuO₂ (*i.e.*, 1.04 V vs 0.98 V at 100 mA cm⁻²). Moreover, S-C₂NA exhibited higher power and current densities of 209 mW cm⁻² and 300 mA cm⁻², respectively, compared to those of Pt/C+RuO₂ (190 mW cm⁻² and 244 mA cm⁻²), P-C₂NA, and C₂NA. No significant voltage drop was observed for S-C₂NA under galvanostatic discharge over 20 h with different current densities, showing better stability for ORR (Figure 4b). The S-C₂NA-based ZABs displayed large specific capacities of 863 and 825 mA h g⁻¹, with corresponding gravimetric energy densities of 958 and 917 Wh kg⁻¹ (normalized to the mass of activated Zn), at current densities of 5 and 25 mA cm⁻², respectively (Figure 4c), comparable or even better than those of Pt/C+RuO₂ and other reported catalysts (Table S5, Supporting Information).^{2,11–13,23,41} Figure 4d displays the galvanodynamic polarization profiles for the rechargeable

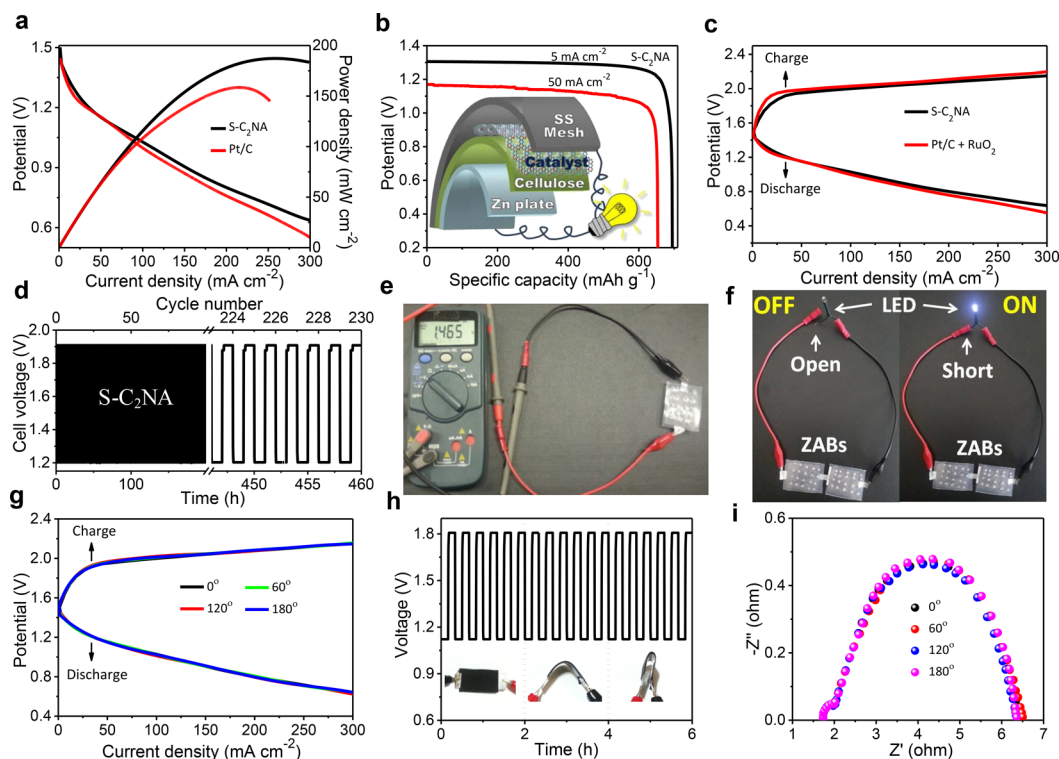


Figure 5. (a) Discharge-voltage and corresponding power-density plots of solid state ZABs with S-C₂N and Pt/C air cathodes. (b) Typical specific capacity of the solid state ZABs using S-C₂NA catalyst at 5 and 50 mA cm⁻² (considering the consumed mass of Zn); the inset displays a schematic diagram of flexible ZAB configuration. (c) Discharge and charge polarization profiles of solid state ZABs with S-C₂NA and Pt/C+RuO₂ as cathodes. (d) Long-term galvanostatic discharging and charging voltage profiles for the flexible rechargeable ZAB with S-C₂NA cathode at 25 mA cm⁻² (cycle time: 2 h/cycle). (e) Photograph of the ZAB showing an open circuit potential of ~1.465 V. (f) A white LED (~2.92 V) before and after being powered by two ZABs in series. (g) Charge and discharge voltage profiles as functions of bending angle. (h) Discharging-charging cycling performance for rechargeable ZAB with S-C₂NA at 10 mA cm⁻² under different bending states. (i) Nyquist plots for tandem ZABs with S-C₂NA electrodes with respect to bending conditions for potential of 1.0 V.

ZABs, which reveals that S-C₂NA has smaller charging and discharging overpotentials than those of Pt/C+RuO₂ (*i.e.*, $\Delta V = 0.70$ V at 25 mA cm⁻², 1.11 V at 100 mA cm⁻² vs 0.83 V at 25 mA cm⁻², 1.32 V at 100 mA cm⁻²), highlighting its superior charge–discharge ability. Figure 4e,f illustrates the long-term cycling stability and reversibility for S-C₂NA air cathode at the current density of 10 mA cm⁻² with a cutoff time of 2 h per cycle. The initial round-trip overpotential was 0.75 V (corresponding voltaic efficiency, 62.1%). After continuous 375 discharge–charge cycles (750 h of operation), a slight increase in round-trip overpotential, to 0.78 V (voltaic efficiency, 60.7%), was observed. Impressively, the S-C₂NA air cathode displays the highest cycle life for a state-of-the-art ZABs with an alkaline catholyte so far (Table S6, Supporting Information). In comparison, the commercial Pt/C+RuO₂ exhibited a significant loss in overpotential after 75 cycles and only 150 h (Figure S19, Supporting Information). The round-trip overpotential increased from 0.97 V for the first cycle to 1.32 V for 75th, with notable decrease in voltaic efficiency from 55.12 to 44.53%. The overall structure and morphology of the S-C₂N aerogels were well maintained after 375 discharge–charge cycles (Figure S20, Supporting Information), highlighting its superior structural stability. The S-C₂NA-based ZABs demonstrates the most alternative efficient air cathodes to expensive noble metals for clean energy conversion and storage applications.

Inspired by the growing interest in flexible and wearable electronic technologies, we fabricated flexible solid-state ZABs

with S-C₂NA coated stainless steel mesh as the air cathode and Zn foil as the anode. A specifically functionalized cellulose membrane gelled with KOH was used as the solid-state electrolyte (Figure S21, Supporting Information). This battery exhibited an OCV of 1.47 V (Figure S22, Supporting Information) and high power density of 187 mW cm⁻² compared to Pt/C (158.4 mW cm⁻²) (Figure 5a) because of its smaller interfacial and charge transfer resistances (Figure S23, Supporting Information). Schematic structure of the solid-state ZAB is shown in the inset of Figure 5b. The specific capacities and corresponding energy densities of the S-C₂NA battery were 695 and 653 mA h g⁻¹, and 862 and 805 Wh kg⁻¹, when normalized to the mass of zinc, at current densities of 5 and 50 mA cm⁻², respectively (Figure 5b). Moreover, the charging–discharging polarization profiles of solid-state ZAB with S-C₂NA displayed comparable performance at lower current densities, but notably outperformed the Pt/C+RuO₂ battery for higher current densities (Figure 5c). The superior performance of S-C₂NA is attributed to the hierarchical holey structure and high ORR and OER activities (Figure 3). Short-interval rechargeability (900 cycles) was also examined to improve the irreversible impacts of the zinc electrode (Figure S24a, Supporting Information).^{3,58} Interestingly, the S-C₂NA battery demonstrated exceptional stability and robustness over 460 h (230 cycles) of continuous operation without exhibiting voltage fade during the charge and discharge processes (Figure 5d). Furthermore, we examined the cycling behavior of the same S-C₂NA electrode with a fresh zinc electrode over a

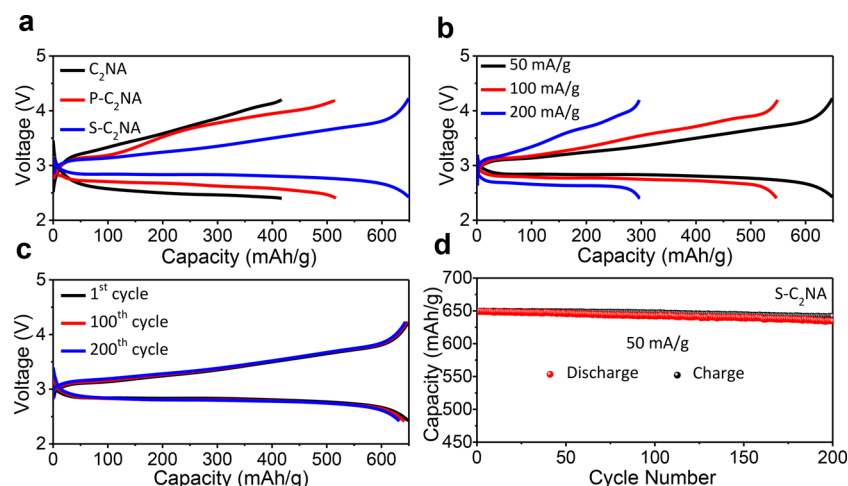


Figure 6. (a) First discharging–charging profiles of Li-O₂ batteries with different 3D C₂N-based-aerogel catalysts for 50 mA g⁻¹. (b) Galvanostatic discharging–charging profiles (first cycle) for the S-C₂NA cathode at current densities in the 50–200 mA g⁻¹ range. (c) Cycling performance with the S-C₂NA cathode in a Li-O₂ cell. (d) Cycling capacity of the S-C₂NA cathode in a Li-O₂ cell.

further 100 h with longer cycle intervals (10 h) under similar conditions (Figure S24b, Supporting Information). No visible changes in voltage polarization were detected for both charge and discharge segments. In contrast, Pt/C+RuO₂ battery displayed inferior cycling stability over 180 h (Figure S25, Supporting Information), resulting significant losses in charge and discharge potentials. This S-C₂NA battery exhibits a rechargeable cycle life and high efficiency that are among the best reported for conventional and flexible ZABs (Tables S6 and S7, Supporting Information).^{2,3,20–23,41,59} The OCV of fabricated ZABs was 1.465 V (Figure 5e). For realistic applications, we showed that a series of two connected ZABs is capable of lighting different light-emitting diodes (LEDs) that function at OCVs of ~2.92 V (Figures 5f, and S26, Video S2, Supporting Information). Moreover, Zn electrodes did not show the formation of dendrites after reactions (Figure S27, Supporting Information). Besides the exceptional cycle life, the S-C₂NA battery exhibited an enormous prospective for flexible and wearable optoelectronic applications. The charge and discharge overpotentials remain almost unchanged for various bending angles compared to the flat configuration (Figure 5g), illustrating the robust mechanical integrity of S-C₂NA battery. The S-C₂NA battery displayed excellent rechargeability and cycling stability under different bending angles without any voltage degradation, confirming linear charge–discharge profiles (Figure 5h). The Nyquist impedance profiles exhibited virtually identical interfacial and charge-transfer resistances at various bending angles (Figure 5i). Moreover, after 2000 cycles of bending, the discharge profile showed only slight voltage polarization, confirming excellent mechanical stability of the flexible ZABs (Figure S28, Supporting Information). This superior performance is a consequence of the structural integrities of the cellulose membrane and the electrodes. Compared with conventional ZABs using liquid electrolytes, this solid-state ZAB provides inspirational opportunities for renewable energy technologies.

With the exceptional bifunctional performance of the S-C₂NA cathodes, we also examined its performance in Li-O₂ batteries. Notably, at 50 mA g⁻¹, S-C₂NA (Figure 6a) exhibited an excellent discharge–charge capacity (648.7 mA h g⁻¹) and lower polarization overpotential than those of P-C₂NA (505 mA h g⁻¹) and C₂NA (417 mA h g⁻¹), illustrating the higher

efficiency of S-C₂NA. The achieved reversible discharge–charge capacities were 648.7, 547.4, and 299.3 mA h g⁻¹ for 50, 100, and 200 mA g⁻¹ current density, respectively (Figure 6b). The sharp increases and decreases in discharge and charge overpotentials indicate the successful nature of the respective charging and discharging reactions. Moreover, long-term cycling experiment revealed no obvious change in overpotential over 200 cycles for 400 h (Figure 6c), confirming the enhanced stability of S-C₂NA in Li-O₂ battery. Figure 6d reveals the retention of >98% of the initial capacity after 200 cycles, displaying outstanding reversibility throughout the deep-cycling process. These results can inspire the fabrication of cost-effective catalysts for metal-air batteries with high intrinsic activities and long cycle lives.

The origin of exceptional catalytic performance and design principles for efficient catalysts were investigated. DFT calculations were used to explore the OER/ORR mechanism of dopant-induced nitrogenated holey structures (X_Y-C₂N, where X and Y are the dopant and doping sites on C₂N, respectively) considering the possible doping and active sites (Figure 7a). For the P and S dopants, we explored favorable doping sites on C₂N by calculating the formation energies (E_f) of X_Y-C₃N₄; calculated E_f and the energetically most favorable structures (C7 and N4 sites are potential active sites) are illustrated in Table S8 (Supporting Information). The results reveal that both P and S prefer the N sites over the C sites; C sites are points of fusion that connect hexagonal rings and induce out-of-plane structural deformation that compensates the structural strain caused by the large dopant. On the other hand, N-site doping preserves the in-plane structure and reduces dopant-induced structural strain by elongating the C–X bond in response to the large dopant. Even though the calculated E_f reveals that both P and S prefer N sites over C sites, all doping substitutions are calculated to be endothermic, with comparable E_f values for P_C-C₂N (1.76 eV) and S_N-C₂N (1.60 eV). Accordingly, we investigated the OER/ORR electrocatalytic activities for the most likely P_N-C₂N and S_N-C₂N structures as well as P_C-C₂N. Following a general method for calculating OER/ORR activity,¹¹ we evaluated the overpotential (η) of the X_Y-C₂N structures to identify the best performing structures and the active sites with lowest $\eta^{\text{OER/ORR}}$. Theoretically, an ideal catalyst facilitates OER/OER

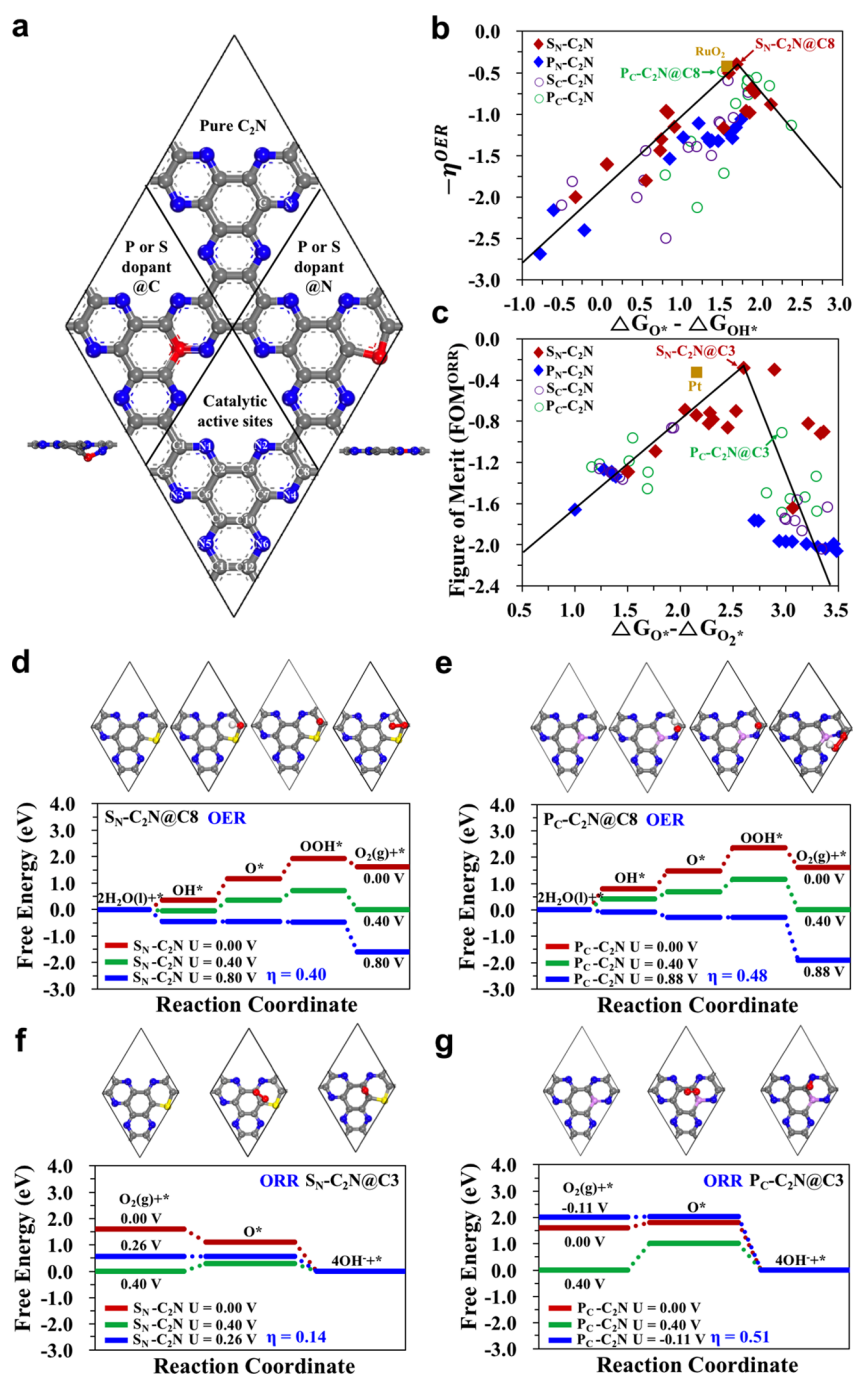


Figure 7. (a) Schematics of the heteroatom-doped nitrogenated holey structures (X_Y-C₂N), with substitutional doping sites in roman characters and the OER/ORR active sites in arabic numerals. (b, c) OER and ORR volcano plots for P_C-C₂N and P_N-C₂N, S_C-C₂N, and S_N-C₂N catalysts. (d, e) Free energy diagrams of S_N-C₂N and P_C-C₂N for the four-electron four-step OER pathway, and (f, g) S_N-C₂N and P_C-C₂N for the four-electron two-step ORR pathway considering the equilibrium and different electrode potentials.

at the equilibrium potential ($U = 0.402$ V in alkaline environment) without an $\eta^{OER/ORR}$. However, real catalytic behavior deviates from the ideal situation because the intermediates have binding energies that require an $\eta^{OER/ORR}$ for spontaneous OER/ORR. Consequently, a lower $\eta^{OER/ORR}$ indicates a thermodynamically superior catalyst. However, in the ORR, η^{ORR} and O₂-adsorption free energy ($\Delta G_{O_2^*}$) are important parameters (Figure S29, Supporting Information), because the O₂-adsorption reactions influence ORR initiation. Although these materials have small η^{ORR} , their ORR activities cannot be revealed because complex O₂-adsorption reactions.

Therefore, we propose an advanced indicator of ORR catalytic activity, namely the ORR figure of merit (FOM^{ORR}) defined by $FOM^{ORR} = -(\eta^{ORR} + \Delta G_{O_2^*})$ (volcano plots for η^{ORR} and FOM^{ORR} in Figure S30, Supporting Information). Detailed descriptions of η^{ORR} , FOM^{ORR} and the reaction free energies (ΔG) are provided in Tables S9–S13 (Supporting Information).

Figure 7b,c displays the OER/ORR volcano plots for different reaction sites on X_Y-C₂N structures based on η^{OER} and FOM^{ORR}. From this theoretical evaluation, S_N-C₂N exhibits the best performance for both the OER/ORR,

followed by P_C-C₂N. This superior OER/ORR performances for S_N-C₂N and P_C-C₂N were observed at the C8 and C3 active sites, respectively, and are ascribed to the electronic and geometric effects of the dopant.¹² The improved electrical conductivities (Figure S13, Supporting Information) and the spin and charge redistributions of the C₂N structures modulated by S or P enable fast electron transfer (*i.e.*, metallic feature with density of states shifted beyond the Fermi level),^{60,61} which boosts their catalytic activities (Figure S31, Supporting Information). In addition, a geometric effect is expected because of the elongated C–S bonds in S_N-C₂N (as consistent with XPS Figure 2f), which relaxes the structural strain of S_C-C₂N in the intermediate states (OH*, O*, and OOH*). In P_C-C₂N, the unsaturated sp³-C and sp³-N geometries formed *via* structural deformation increase the activity of vicinal sites of dopant by stabilizing the intermediate states. Figure 7d–g displays free-energy diagrams based on the four-electron mechanism^{11,12} for S_N-C₂N and P_C-C₂N at their best-performing active sites (C8 and C3 for both OER and ORR, respectively). The ORR proceeds *via* a two-step or four-step pathway⁶² depending on the relative stabilities of the intermediates, and we confirmed that X_Y-C₂N follows the four-electron two-step pathway in the rate-limiting ORR process (see OER/ORR mechanism and Figure S29, Supporting Information), in good agreement with experimental results (Figure 3a,b). The calculated $\eta^{\text{OER/ORR}}$ correlated with the largest ΔG values among all the elementary steps at the equilibrium potential, $U = 0.40$ V. The obtained η^{OER} and η^{ORR} for S_N-C₂N (P_C-C₂N) are 0.40 V (0.48 V) and 0.14 V (0.51 V), respectively, comparable or outperform the noble-metal catalysts for OER (RuO₂ \sim 0.43 V)⁶³ and ORR (Pt \sim 0.45 V).⁴¹ The endothermic uphill from O* to OOH* is the rate-determining step for OER. Overall, the observed outstanding OER/ORR catalytic performance of these materials follows the order: S_N-C₂N > P_C-C₂N > S_C-C₂N > P_N-C₂N. This confirms that S_N-C₂N, with excellent $\eta^{\text{OER/ORR}}$ values, is the best candidate for metal-free bifunctional catalyst. The superior ORR and OER activities of C₂N catalysts might be due to asymmetric spins and charge densities of their carbon atoms through N, S, or P atoms.⁴⁷ Moreover, S has comparable electronegativity (2.58) to that of carbon (2.55), which reduces energy barriers that involve its highest occupied and lowest unoccupied molecular orbital (HOMO/LUMO), and lead to modified electronic configurations.⁶⁴ Besides, the construction of S–N bonds reinforces ORR active sites (consistent with XPS). The transformations of the O₂²⁻, and O₂⁻ intermediates, and the adsorptions of OH⁻ and oxygen (Figure S6, Supporting Information) induce positive charges on carbon atoms that enhance OER activity.⁴¹ Thus, DFT calculations are well consistent with the experimental results, highlighting the electronic and geometric effects that boost OER/ORR performance.

CONCLUSIONS

In summary, hierarchical sulfur-modulated 3D holey C₂N aerogels as bifunctional oxygen catalysts for rechargeable Zn-air and Li-O₂ batteries have been constructed *via* a facile scalable amination and polymerization strategy. Benefiting from its 3D holey structure and ultrahigh surface area (1943 m²g⁻¹), S-C₂N aerogels exhibit exceptional bifunctional ORR and OER performance ($\Delta E = 0.65$ V) outperforming noble-metal (Pt/C and RuO₂) benchmarks in relation to current densities, lower overpotentials, stabilities, and reaction kinetics.

DFT calculations reveal that the heteroatom-induced charge and spin density polarization affects and amends the sorption free energies involving reaction intermediates at the N- and defect-rich sites, facilitating excellent ORR and OER activities. The S-C₂NA-based ZABs, using both aqueous and solid-state electrolytes, exhibit high energy densities and exceptionally long cycle lives of over 750 and 460 h, respectively, and outperform most recently reported ZABs. The superior mechanical flexibility and activity of S-C₂NA and the solid electrolyte resolve persistent problems of dendrite formation, zincate loss, and low cell voltage, highlighting their great potential for green energy generation and smart wearable storage applications.

METHODS

Chemicals and Materials. Chloroanilic acid (C₆H₂Cl₂O₄), ethylenediamine (NH₂CH₂CH₂NH₂), L-alanine (C₃H₇NO₂), L-cysteine (HSCH₂CH(NH₂)CO₂H), L-phosphoserine (C₃H₈NO), ammonium peroxydisulfate ((NH₄)₂S₂O₈), and ammonium phosphate ((NH₄)₃PO₄) were purchased from Sigma-Aldrich. Sulfuric acid (H₂SO₄) was purchased from Daejung Chemicals. All reagents are of analytical reagents grade and employed without additional refinement.

Fabrication of 3D Holey S-C₂N Aerogels. The 3D holey S-C₂N aerogels were fabricated by a facile amination and polymerization process in the presence of chloroanilic acid. Typically, 0.5 g of chloroanilic acid was mixed with 5 g of ethylenediamine, followed by addition of a few drops of sulfuric acid with vigorous stirring in an ice-bath for 5 min. The resultant solutions were then endorsed to warm to room temperature before being treated at 80 °C for 12 h to ensure complete amination of chloroanilic acid. The resulted solid product was collected by vacuum filtration, washed with degassed ethanol and diethyl ether, followed by subsequent freeze-drying for 24 h to afford the brownish-black hexaaminobenzene complex. In a typical experiment (formation of the S-C₂N aerogels), hexaaminobenzene and chloroanilic acid were redispersed in 1-methyl-2-pyrrolidinone (1:1.2 wt %), followed by addition of L-alanine and L-cysteine with vigorous stirring at room temperature. A few drops of ammonium peroxydisulfate (ammonium phosphate for phosphorus case) and sulfuric acid were slowly poured. The resulting solutions were heated at 120 °C for 8 h and then cooled to room temperature. The resulting hydrogel was subsequently washed with methanol and deionized water (twice), followed by freeze-drying for 20 h. Finally, the obtained aerogels were annealed at 200 °C for 30 min under N₂ (150 sccm) at a ramping rate of 2 °C min⁻¹ to yield the S-C₂N aerogels. For comparison, pristine C₂N and P-C₂N aerogels were also prepared with the similar procedure without L-cysteine and addition of L-phosphoserine, respectively. The aerogel dimensions were controlled by varying the quantity of the employed precursors and solvents.

The Hydroxide-Conductive Cellulose Membrane. *Pinus radiata* wood powder sieved at 60 meshes was considered in this experiment. The wood powder was solvent extracted for 6 h using Soxhlet apparatus with a 2:1 (v/v) mixture of ethanol and toluene. Further removal of lignin was performed with acidified sodium chlorite at 70 °C until white pulp was obtained. The resulting pulp was then treated overnight with potassium hydroxide (6 wt %), followed by heating at 80 °C for 2 h to leach the hemicelluloses. The treated pulp was thoroughly washed with DI water to remove soluble residues and ground by a PFI mill (uprising up to 30,000) to obtain the cellulose nanofibers. The cellulose nanofibers were functionalized using didecylmethylammonium chloride (DDAC) by redispersion in DI water, followed by the addition of 10% DDAC solution, and the mixture stirred overnight. Multiple centrifugations and washings with ethanol and DI water removed the residual DDAC. The cellulose film (functionalized by quaternary ammonium moieties) was collected by vacuum filtration and dried at room temperature for 6 h. Cross-linking was subsequently performed at 60 °C for 24 h under vacuum. The resulting cellulose film (40–50 μm) was hydroxide exchanged in 6 M

KOH for 24 h; the hydroxide-exchanged cellulose membrane was then washed and soaked in DI water.

ASSOCIATED CONTENT

Supporting Information

The Supporting Information is available free of charge on the ACS Publications website at DOI: 10.1021/acsnano.7b07473.

Detailed experimental methods, structural analysis (XRD, TGA, FTIR, XPS), electrochemical analysis (CV spectra, chronoamperometric plots, RRDE, tables, and DFT calculations details, and data (PDF)

Video S1: Oxygen evolution performance from S-C₂NA on carbon paper as the working electrode at operating potential of 1.53 V. Video S2: Demonstrating the powering of a red LED by a series of two ZABs with S-C₂A as the air cathode under ON and OFF conditions (ZIP)

AUTHOR INFORMATION

Corresponding Authors

*E-mail: junggho@hanyang.ac.kr.

*E-mail: sulee@hanyang.ac.kr.

ORCID

Chi Ho Lee: 0000-0002-0127-0059

Sang Uck Lee: 0000-0001-9596-2349

Jung-Ho Lee: 0000-0002-6731-3111

Author Contributions

These authors contributed equally to this work.

Notes

The authors declare no competing financial interest.

ACKNOWLEDGMENTS

This work was supported by a National Research Foundation of Korea (NRF) grant funded by the Korean government (MSIP) (no. 2017R1A2B3006941). S.U.L. thanks the Basic Science Research Program through the National Research Foundation of Korea (NRF) funded by the Ministry of Science, ICT, and Future Planning (NRF-2015R1C1A1A02036670).

REFERENCES

- (1) Fu, G.; Chen, Y.; Cui, Z.; Li, Y.; Zhou, W.; Xin, S.; Tang, Y.; Goodenough, J. Novel Hydrogel-Derived Bifunctional Oxygen Electrocatalyst for Rechargeable Air Cathodes. *Nano Lett.* **2016**, *16*, 6516–6522.
- (2) Su, C.; Cheng, H.; Li, W.; Liu, Z.; Li, N.; Hou, Z.; Bai, F.; Zhang, H.; Ma, T. Atomic Modulation of FeCo–Nitrogen–Carbon Bifunctional Oxygen Electrodes for Rechargeable and Flexible All-Solid-State Zinc–Air Battery. *Adv. Energy Mater.* **2017**, *7*, 1602420.
- (3) Fu, F.; Hassan, J.; Li, J.; Lee, D.; Ghannoum, A.; Lui, G.; Hoque, M.; Chen, Z. Flexible Rechargeable Zinc–Air Batteries Through Morphological Emulation of Human Hair Array. *Adv. Mater.* **2016**, *28*, 6421–6428.
- (4) Aurbach, D.; McCloskey, B.; Nazar, L.; Bruce, P. Advances In Understanding Mechanisms Underpinning Lithium–Air Batteries. *Nat. Energy* **2016**, *1*, 16128.
- (5) Cheng, X.; Hou, T.; Zhang, R.; Peng, H.; Zhao, C.; Huang, J.; Zhang, Q. Dendrite-Free Lithium Deposition Induced by Uniformly Distributed Lithium Ions for Efficient Lithium Metal Batteries. *Adv. Mater.* **2016**, *28*, 2888–2895.
- (6) Liu, B.; Yan, P.; Xu, W.; Zheng, J.; He, Y.; Luo, L.; Bowden, M.; Wang, C.; Zhang, J. Electrochemically Formed Ultrafine Metal Oxide

Nanocatalysts for High-Performance Lithium–Oxygen Batteries. *Nano Lett.* **2016**, *16*, 4932–4939.

- (7) Liu, Z.; Cheng, H.; Li, N.; Ma, T.; Su, Y. ZnCo₂O₄ Quantum Dots Anchored On Nitrogen-Doped Carbon Nanotubes As Reversible Oxygen Reduction/Evolution Electrocatalysts. *Adv. Mater.* **2016**, *28*, 3777–3784.

- (8) Liu, J.; Guan, C.; Zhou, C.; Fan, Z.; Ke, Q.; Zhang, G.; Liu, C.; Wang, J. A Flexible Quasi-Solid-State Nickel–Zinc Battery With High Energy and Power Densities Based on 3D Electrode Design. *Adv. Mater.* **2016**, *28*, 8732–8739.

- (9) Li, L.; Liu, C.; He, G.; Fan, D.; Manthiram, A. Hierarchical Pore-In-Pore and Wire-In-Wire Catalysts for Rechargeable Zn– and Li–Air Batteries With Ultra-Long Cycle Life and High Cell Efficiency. *Energy Environ. Sci.* **2015**, *8*, 3274–3282.

- (10) Shinde, S.; Yu, J.; Song, J.; Nam, Y.; Kim, D.; Lee, J. Highly Active and Durable Carbon Nitride Fibers As Metal-Free Bifunctional Oxygen Electrodes for Flexible Zn–Air Batteries. *Nanoscale Horiz.* **2017**, *2*, 333–341.

- (11) Zhang, J.; Zhao, Z.; Xia, Z.; Dai, L. A Metal-Free Bifunctional Electrocatalyst for Oxygen Reduction and Oxygen Evolution Reactions. *Nat. Nanotechnol.* **2015**, *10*, 444–452.

- (12) Shinde, S.; Lee, C.; Sami, A.; Kim, D.; Lee, S.; Lee, J. Scalable 3D Carbon Nitride Sponge As An Efficient Metal-Free Bifunctional Oxygen Electrocatalyst for Rechargeable Zn–Air Batteries. *ACS Nano* **2017**, *11*, 347–357.

- (13) Li, Y.; Gong, M.; Liang, Y.; Feng, J.; Kim, J.; Wang, H.; Hong, G.; Zhang, B.; Dai, H. Advanced Zinc–Air Batteries Based on High-Performance Hybrid Electrocatalysts. *Nat. Commun.* **2013**, *4*, 1805.

- (14) Fu, G.; Cui, Z.; Chen, Y.; Li, Y.; Tang, Y.; Goodenough, J. Ni₃Fe–N Doped Carbon Sheets As a Bifunctional Electrocatalyst for Air Cathodes. *Adv. Energy Mater.* **2017**, *7*, 1601172.

- (15) Li, G.; Wang, X.; Fu, J.; Li, J.; Park, M.; Zhang, Y.; Lui, G.; Chen, Z. Pomegranate-Inspired Design of Highly Active and Durable Bifunctional Electrocatalysts for Rechargeable Metal–Air Batteries. *Angew. Chem., Int. Ed.* **2016**, *55*, 4977–4982.

- (16) Lu, Y.; Xu, Z.; Gasteiger, H.; Chen, S.; Hamad-Schifferli, K.; Horn, Y. Platinum–Gold Nanoparticles: A Highly Active Bifunctional Electrocatalyst for Rechargeable Lithium–Air Batteries. *J. Am. Chem. Soc.* **2010**, *132*, 12170–12171.

- (17) Li, L.; Manthiram, A. Long-Life, High-Voltage Acidic Zn–Air Batteries. *Adv. Energy Mater.* **2016**, *6*, 1502054.

- (18) Li, L.; Dai, H. Recent Advances in Zinc–Air Batteries. *Chem. Soc. Rev.* **2014**, *43*, 5257–5275.

- (19) Chen, Y.; Freunberger, S.; Peng, Z.; Fontaine, O.; Bruce, P. Charging a Li–O₂ Battery Using A Redox Mediator. *Nat. Chem.* **2013**, *5*, 489–494.

- (20) Fu, J.; Lee, D.; Hassan, F.; Yang, L.; Bai, Z.; Park, M.; Chen, Z. Flexible High-Energy Polymer–Electrolyte-Based Rechargeable Zinc–Air Batteries. *Adv. Mater.* **2015**, *27*, 5617–5622.

- (21) Fu, K.; Gong, Y.; Liu, B.; Zhu, Y.; Xu, S.; Yao, Y.; Luo, W.; Wang, C.; Lacey, S.; Dai, J.; Chen, Y.; Mo, Y.; Wachsman, E.; Hu, L. Toward Garnet Electrolyte-Based Li Metal Batteries: An Ultrathin, Highly Effective, Artificial Solid-State Electrolyte/Metallic Li Interface. *Sci. Adv.* **2017**, *3*, e1601659.

- (22) Xu, J.; Gao, P.; Zhao, T. Non-Precious Co₃O₄ Nano-Rod Electrocatalyst for Oxygen Reduction Reaction in Anion-Exchange Membrane Fuel Cells. *Energy Environ. Sci.* **2012**, *5*, 5333–5339.

- (23) Meng, F.; Zhong, H.; Bao, D.; Yan, J.; Zhang, X. *In Situ* Coupling of Strung Co₄N and Intertwined N–C Fibers Toward Free-Standing Bifunctional Cathode for Robust, Efficient, and Flexible Zn–Air Batteries. *J. Am. Chem. Soc.* **2016**, *138*, 10226–10231.

- (24) Petrie, J.; Cooper, V.; Freeland, J.; Meyer, T.; Zhang, Z.; Lutterman, D.; Lee, H. Enhanced Bifunctional Oxygen Catalysis in Strained LaNiO₃ Perovskites. *J. Am. Chem. Soc.* **2016**, *138*, 2488–2491.

- (25) Jung, J.; Risch, M.; Park, S.; Kim, M.; Nam, G.; Jeong, H.; Horn, Y.; Cho, J. Optimizing Nanoparticle Perovskite for Bifunctional Oxygen Electrocatalysis. *Energy Environ. Sci.* **2016**, *9*, 176–183.

- (26) Cheng, F.; Shen, J.; Peng, B.; Pan, Y.; Tao, Z.; Chen, J. Rapid Room-Temperature Synthesis of Nanocrystalline Spinel As Oxygen Reduction and Evolution Electrocatalysts. *Nat. Chem.* **2011**, *3*, 79–84.
- (27) Chen, Z.; Yu, A.; Higgins, D.; Li, H.; Wang, H.; Chen, Z. Highly Active and Durable Core-Corona Structured Bifunctional Catalyst for Rechargeable Metal-Air Battery Application. *Nano Lett.* **2012**, *12*, 1946–1952.
- (28) Gong, K.; Du, F.; Xia, Z.; Durstock, M.; Dai, L. Nitrogen-Doped Carbon Nanotube Arrays With High Electrocatalytic Activity for Oxygen Reduction. *Science* **2009**, *323*, 760–764.
- (29) Li, B.; Geng, D.; Lee, X.; Ge, X.; Chai, J.; Wang, Z.; Zhang, J.; Liu, Z.; Hor, T. S. A.; Zong, Y. Eggplant-Derived Microporous Carbon Sheets: Towards Mass Production of Efficient Bifunctional Oxygen Electrocatalysts at Low Cost for Rechargeable Zn–Air Batteries. *Chem. Commun.* **2015**, *51*, 8841–8844.
- (30) Geng, D.; Ding, N.; Hor, T. S. A.; Chien, S.; Liu, Z.; Wu, D.; Sun, X.; Zong, Y. From Lithium–Oxygen to Lithium–Air Batteries: Challenges and Opportunities. *Adv. Energy Mater.* **2016**, *6*, 1502164.
- (31) Sakaushi, K.; Antonietti, M. Carbon- and Nitrogen-Based Organic Frameworks. *Acc. Chem. Res.* **2015**, *48*, 1591–1600.
- (32) Cote, A.; Benin, A.; Ockwig, N.; O’Keeffe, M.; Matzger, A.; Yaghi, O. Porous, Crystalline, Covalent Organic Frameworks. *Science* **2005**, *310*, 1166–1170.
- (33) Wang, Y.; Wang, X.; Antonietti, M. Polymeric Graphitic Carbon Nitride As a Heterogeneous Organocatalyst: From Photochemistry to Multipurpose Catalysis to Sustainable Chemistry. *Angew. Chem., Int. Ed.* **2012**, *51*, 68–89.
- (34) Xu, Y.; Jin, S.; Xu, H.; Nagai, A.; Jiang, D. Conjugated Microporous Polymers: Design, Synthesis and Application. *Chem. Soc. Rev.* **2013**, *42*, 8012–8031.
- (35) Ma, T.; Dai, S.; Jaroniec, M.; Qiao, S. Graphitic Carbon Nitride Nanosheet–Carbon Nanotube Three-Dimensional Porous Composites As High-Performance Oxygen Evolution Electrocatalysts. *Angew. Chem.* **2014**, *126*, 7409–7413.
- (36) Wichterle, O.; Lim, D. Hydrophilic Gels for Biological Use. *Nature* **1960**, *185*, 117–118.
- (37) Biener, J.; Stadermann, M.; Suss, M.; Worsley, M.; Biener, M.; Rose, K.; Baumann, T. Advanced Carbon Aerogels for Energy Applications. *Energy Environ. Sci.* **2011**, *4*, 656–667.
- (38) Pierre, A.; Pajonk, G. Chemistry of Aerogels and Their Applications. *Chem. Rev.* **2002**, *102*, 4243–4266.
- (39) Wang, H.; Xu, Z.; Yi, H.; Wei, H.; Guo, Z.; Wang, X. One-Step Preparation of Single-Crystalline Fe₂O₃ Particles/Graphene Composite Hydrogels As High Performance Anode Materials for Supercapacitors. *Nano Energy* **2014**, *7*, 86–96.
- (40) Chen, Z.; To, J.; Wang, C.; Lu, Z.; Liu, N.; Chortos, A.; Pan, L.; Wei, F.; Cui, Y.; Bao, Z. A Three-Dimensionally Interconnected Carbon Nanotube-Conducting Polymer Hydrogel Network for High-Performance Flexible Battery Electrodes. *Adv. Energy Mater.* **2014**, *4*, 1400207.
- (41) Liu, Q.; Wang, Y.; Dai, L.; Yao, J. Scalable Fabrication of Nanoporous Carbon Fiber Films As Bifunctional Catalytic Electrodes for Flexible Zn–Air Batteries. *Adv. Mater.* **2016**, *28*, 3000–3006.
- (42) Mahmood, J.; Lee, E.; Jung, M.; Shin, D.; Jeon, I.; Jung, S.; Choi, H.; Seo, J.; Bae, S.; Sohn, S.; Park, N.; Oh, J.; Shin, H.; Baek, J. Nitrogenated Holey Two-Dimensional Structures. *Nat. Commun.* **2015**, *6*, 6486.
- (43) Wu, H.; Geng, J.; Ge, H.; Guo, Z.; Wang, Y.; Zheng, G. Egg-Derived Mesoporous Carbon Microspheres As Bifunctional Oxygen Evolution and Oxygen Reduction Electrocatalysts. *Adv. Energy Mater.* **2016**, *6*, 1600794.
- (44) Ahn, S.; Yu, X.; Manthiram, A. Wiring Fe–N_x-Embedded Porous Carbon Framework Onto 1D Nanotubes for Efficient Oxygen Reduction Reaction in Alkaline and Acidic Media. *Adv. Mater.* **2017**, *29*, 1606534.
- (45) Ai, K.; Liu, Y.; Ruan, C.; Lu, L.; Lu, G. Sp² C-Dominant N-Doped Carbon Sub-Micrometer Spheres With a Tunable Size: A Versatile Platform for Highly Efficient Oxygen-Reduction Catalysts. *Adv. Mater.* **2013**, *25*, 998–1003.
- (46) Palaniselvam, T.; Valappil, M.; Illathvalappil, R.; Kurungot, S. Nanoporous Graphene by Quantum Dots Removal From Graphene and Its Conversion to a Potential Oxygen Reduction Electrocatalyst via Nitrogen Doping. *Energy Environ. Sci.* **2014**, *7*, 1059–1067.
- (47) Choi, C.; Park, S.; Woo, S. Binary and Ternary Doping of Nitrogen, Boron, and Phosphorus Into Carbon for Enhancing Electrochemical Oxygen Reduction Activity. *ACS Nano* **2012**, *6*, 7084–7091.
- (48) Ma, T.; Ran, J.; Dai, S.; Jaroniec, M.; Qiao, S. Phosphorus-Doped Graphitic Carbon Nitrides Grown *in Situ* on Carbon-Fiber Paper: Flexible and Reversible Oxygen Electrodes. *Angew. Chem., Int. Ed.* **2015**, *54*, 4646–4650.
- (49) Sivanantham, A.; Ganesan, P.; Shanmugam, S. Hierarchical NiCo₂S₄ Nanowire Arrays Supported on Ni Foam: An Efficient and Durable Bifunctional Electrocatalyst for Oxygen and Hydrogen Evolution Reactions. *Adv. Funct. Mater.* **2016**, *26*, 4661–4672.
- (50) Kim, J.; Lee, S.; Chen, S.; Shao-Horn, Y. Synthesis and Oxygen Reduction Reaction Activity of Atomic and Nanoparticle Gold on Thiol-Functionalized Multiwall Carbon Nanotubes. *Electrochem. Solid-State Lett.* **2011**, *14*, B105–B109.
- (51) Luo, Z.; Yang, D.; Qi, G.; Shang, J.; Yang, H.; Wang, Y.; Yuwen, L.; Yu, T.; Huang, W.; Wang, L. Microwave-Assisted Solvothermal Preparation of Nitrogen and Sulfur Co-Doped Reduced Graphene Oxide and Graphene Quantum Dots Hybrids for Highly Efficient Oxygen Reduction. *J. Mater. Chem. A* **2014**, *2*, 20605–20611.
- (52) Sheng, Z.; Shao, L.; Chen, J.; Bao, W.; Wang, F.; Xia, X. Catalyst-Free Synthesis of Nitrogen-Doped Graphene *via* Thermal Annealing Graphite Oxide With Melamine and Its Excellent Electrocatalysis. *ACS Nano* **2011**, *5*, 4350–4358.
- (53) Luo, Z.; Lim, S.; Tian, Z.; Shang, J.; Lai, L.; MacDonald, B.; Fu, C.; Shen, Z.; Yu, T.; Lin, J. Pyridinic N Doped Graphene: Synthesis, Electronic Structure, and Electrocatalytic Property. *J. Mater. Chem.* **2011**, *21*, 8038–8044.
- (54) Lai, L.; Potts, J.; Zhan, D.; Wang, L.; Poh, C.; Tang, C.; Gong, H.; Shen, Z.; Lin, J.; Ruoff, R. Exploration of the Active Center Structure of Nitrogen-Doped Graphene-Based Catalysts for Oxygen Reduction Reaction. *Energy Environ. Sci.* **2012**, *5*, 7936–7942.
- (55) Choi, C.; Lim, H.; Chung, M.; Park, J.; Shin, H.; Kim, H.; Woo, S. Long-Range Electron Transfer Over Graphene-Based Catalyst for High-Performing Oxygen Reduction Reactions: Importance of Size, N-Doping, and Metallic Impurities. *J. Am. Chem. Soc.* **2014**, *136*, 9070–9077.
- (56) Pels, J.; Kapteijn, F.; Moulijn, J.; Zhu, Q.; Thomas, K. Evolution of Nitrogen Functionalities in Carbonaceous Materials During Pyrolysis. *Carbon* **1995**, *33*, 1641–1653.
- (57) Chen, P.; Zhou, T.; Xing, L.; Xu, K.; Tong, Y.; Xie, H.; Zhang, L.; Yan, W.; Chu, W.; Wu, C.; Xie, Y. Atomically Dispersed Iron-Nitrogen Species As Electrocatalysts for Bifunctional Oxygen Evolution and Reduction Reactions. *Angew. Chem., Int. Ed.* **2017**, *56*, 610–614.
- (58) Xu, Y.; Zhang, Y.; Guo, Z.; Ren, J.; Wang, Y.; Peng, H. Flexible, Stretchable, and Rechargeable Fiber-Shaped Zinc–Air Battery Based on Cross-Stacked Carbon Nanotube Sheets. *Angew. Chem., Int. Ed.* **2015**, *54*, 15390–15394.
- (59) Fu, J.; Zhang, J.; Song, X.; Zarrin, H.; Tian, X.; Qiao, J.; Rasen, L.; Lib, K.; Chen, Z. A Flexible Solid-State Electrolyte for Wide-Scale Integration of Rechargeable Zinc–Air Batteries. *Energy Environ. Sci.* **2016**, *9*, 663–670.
- (60) Chai, G.; Hou, Z.; Shu, D.; Ikeda, T.; Terakura, K. Active Sites and Mechanisms for Oxygen Reduction Reaction on Nitrogen-Doped Carbon Alloy Catalysts: Stone-Wales Defect and Curvature Effect. *J. Am. Chem. Soc.* **2014**, *136*, 13629–13640.
- (61) Pei, Z.; Gu, J.; Wang, Y.; Tang, Z.; Liu, Z.; Huang, Y.; Huang, Y.; Zhao, J.; Chen, Z.; Zhi, C. Component Matters: Paving the Roadmap Toward Enhanced Electrocatalytic Performance of Graphitic C₃N₄-Based Catalysts *via* Atomic Tuning. *ACS Nano* **2017**, *11*, 6004–6014.
- (62) Dai, L.; Xue, Y.; Qu, L.; Choi, H.; Baek, J. Metal-Free Catalysts for Oxygen Reduction Reaction. *Chem. Rev.* **2015**, *115*, 4823–4892.

(63) Mao, S.; Wen, Z.; Huang, T.; Hou, Y.; Chen, J. High-Performance Bifunctional Electrocatalysts of 3D Crumpled Graphene-Cobalt Oxide Nanohybrids for Oxygen Reduction and Evolution Reactions. *Energy Environ. Sci.* **2014**, *7*, 609–616.

(64) Liang, J.; Jiao, Y.; Jaroniec, M.; Qiao, S. Sulfur and Nitrogen Dual-Doped Mesoporous Graphene Electrocatalyst for Oxygen Reduction With Synergistically Enhanced Performance. *Angew. Chem., Int. Ed.* **2012**, *51*, 11496–11500.